Atmos. Chem. Phys., 26, 11771–11784, 2026
https://doi.org/10.5194/acp-26-11771-2026

Atmospheric Chemistry and Physics
Open Access
EGU

Measurement report: Dust Transport and Local Anthropogenic Emissions Differently Shape Atmospheric Ice-Nucleating Particles in an Industrial Urban Atmosphere

Jiawei Yang[1], Jingchuan Chen[1], Jie Chen[2], Zeyu Feng[1], Wenxu Fang[1], Yanting Qiu[1], Junrui Wang[1], Ruiqi Man[1], Taomou Zong[1], Yuechen Liu[4], Zhijun Wu[1,3], Ning Tang[5], and Min Hu[1]

[1]State Key Laboratory of Regional Environment and Sustainability, International Joint Research Center for Atmospheric Research (IJRC), Institute of Carbon Neutrality, College of Environmental Sciences and Engineering, Peking University, Beijing 100871, China
[2]Institute for Atmospheric and Climate Science, ETH Zürich, 8092 Zurich, Switzerland
[3]Collaborative Innovation Center of Atmospheric Environment and Equipment Technology, Nanjing University of Information Science and Technology, Nanjing 210044, China
[4]National Institute of Metrology, Beijing 100029, China
[5]Institute of Nature and Environmental Technology, Kanazawa University, Kanazawa, Japan

Correspondence: Zhijun Wu (zhijunwu@pku.edu.cn)

Received: 20 January 2026 – Revised: 2 June 2026 – Accepted: 7 July 2026 – Published: 19 August 2026

Abstract. Atmospheric ice-nucleating particles (INPs) are vital for cloud formation, yet the importance of INPs from anthropogenic sources remains poorly understood. We conducted a month-long winter field campaign in Taiyuan (China), a heavily industrialized city, to quantify INP concentrations (N_{INP}) and ice nucleation active site density (n_s) of immersion mode INPs, alongside particle size distributions and chemical compositions. Our results indicate that N_{INP} ranged from 0.05 to 13.37 L^{-1} at and above −15 °C, corresponding to n_s values of 10^5–10^7 m^{-2}. During the identified desert dust event, both N_{INP} (7.47 L^{-1}; 95 % confidence interval (CI): 6.64–8.41 L^{-1}) and n_s (1.57×10^7 m^{-2}) were substantially higher than during the remaining observation periods without clear desert-dust intrusion (0.61 L^{-1} and 9.52×10^5 m^{-2}, respectively), highlighting the strong influence of long-range transported desert dust. In contrast, during pollution periods, N_{INP} showed only weak correlations with urban aerosol components such as sulfate (SO_4^{2-}), nitrate (NO_3^-), and organic carbon (OC) ($|r| < 0.3$). Positive matrix factorization (PMF) identified five $PM_{2.5}$ source factors: industrial emissions, dust-related particles, secondary aerosols, coal combustion and traffic emissions, and fireworks. Although these factors dominated the $PM_{2.5}$ mass, they showed no significant covariation with N_{INP}. During this winter campaign, N_{INP} variability in Taiyuan was characterized by strong enhancement during the identified desert dust event and weak associations with the major $PM_{2.5}$ source factors during the remaining observation periods.

1 Introduction

Atmospheric ice-nucleating particles (INPs) play a critical role in cloud formation, cloud radiative properties and precipitation through heterogeneous ice nucleation (Lohmann and Feichter, 2005; IPCC, 2014; Lohmann et al., 2016). Although INPs constitute a minute fraction of ambient aerosols under natural conditions (approximately 1 in 10^5 ambient particles in the free troposphere, DeMott et al., 2010), their ability to modulate cloud properties and lifetimes has received substantial scientific interest. Heterogeneous ice nucleation is generally understood to occur through four mechanisms: deposition ice nucleation, condensation freezing, immersion freezing and contact freezing (Hoose and Möhler,

2012; Vali et al., 2015). In addition, recent studies have suggested that under water-subsaturated conditions, pore condensation and freezing (PCF) may provide a more realistic description of atmospheric ice nucleation than classical deposition nucleation in some cases (Marcolli, 2014; David et al., 2019). Among these, immersion freezing has been widely reported to be the most important ice nucleation mechanism for mixed-phase clouds (Ansmann et al., 2008; Murray et al., 2012; Westbrook and Illingworth, 2013).

The urban atmosphere is characterized by intensive anthropogenic activities, diverse aerosol emission sources, elevated aerosol loadings, and complex chemical compositions. However, the key factors controlling atmospheric INP concentrations in such environments, including aerosol composition, size, and source characteristics, remain uncertain (Kanji et al., 2017). Previous studies in Beijing and Tokyo demonstrated that INP concentrations often show no significant correlations with black carbon (BC) or $PM_{2.5}$ mass, or the number concentration of particles larger than 0.5 µm during air pollution episodes (Chen et al., 2018; Tobo et al., 2020; Zhang et al., 2022). This suggests that typical urban pollution aerosols are generally inefficient INPs.

However, this observation contrasts with laboratory and field evidence showing that some anthropogenic particles can exhibit immersion-mode ice-nucleating activity. These include certain fly ash, metallic/mineral particles, and other industrial dusts associated with coal combustion and manufacturing activities (Toll et al., 2024). By contrast, the contribution of soot particles to atmospheric INPs in the immersion mode has been suggested to be negligible in many cases (Kanji et al., 2020). Moreover, biomass burning represents another potential source, with agricultural fires near Mexico City reported to induce freezing at temperatures above −15 °C, likely due to the presence of associated biological particles (McCluskey et al., 2014; Jahn et al., 2020; Cabrera-Segoviano et al., 2022). The complexity of urban INPs is further exemplified by observations in New Delhi, where INP concentrations correlated moderately ($r = 0.52$) with BC during fog episodes, indicating that particle composition and meteorological conditions may modulate INP activity (Wagh et al., 2021). This gap between laboratory potential and field observations indicates that urban INP variability may be governed by specific high-efficiency contributors rather than total aerosol mass or number concentrations. Therefore, mineral dust and biological particles, which have long been established as the most potent atmospheric INPs, require careful consideration even in heavily industrialized areas.

Mineral dust is widely recognized as the most important atmospheric INP due to its vast global emissions, estimated at up to $\sim 5000\,\mathrm{Tg\,yr^{-1}}$ (Engelstaedter et al., 2006). Its intrinsically high ice-nucleating activity at temperatures below −8 °C is primarily attributed to specific mineral components such as K-feldspar, which has been systematically identified as a key active species in laboratory settings (Atkinson et al., 2013; Augustin-Bauditz et al., 2014; Zolles et al., 2015). In the context of East Asia, mineral dust transported from northwestern deserts can substantially enhance INP concentrations in downwind urban areas, with ice-nucleating efficiencies comparable to those reported for Saharan dust (Price et al., 2018; Reicher et al., 2019; Chen et al., 2021). Furthermore, the influence of dust in urban environments is not limited to long-range natural transport; anthropogenic dust may also contribute to atmospheric INPs in some urban and peri-urban regions, although direct field evidence remains limited (Chen et al., 2024).

In comparison to mineral dust, aerosols of biological origin, such as pollen, fungal spores, proteins, and other macromolecular organics can nucleate ice at relatively warmer temperatures, often above −15 °C (Pummer et al., 2015; Polen et al., 2016; Kanji et al., 2017). While these bioaerosols may be less abundant by mass than mineral dust, their exceptional ice-nucleating efficiency means that even a small population can dominate the urban INP budget at the early stages of cloud glaciation.

Although considerable progress has been made in identifying both natural and anthropogenic sources of atmospheric INPs, their formation pathways and source attributions in urban environments remain poorly constrained due to the complex mixture of aerosol types and variable emission patterns. To address this gap, a comprehensive winter field campaign was conducted in Taiyuan, a representative industrial city in northern China, over a one-month period. Taiyuan frequently experiences severe particulate pollution and episodic dust events, positioning it as an ideal location to investigate the combined effects of anthropogenic and natural emissions. In this study, the number concentration of immersion mode INP (N_{INP}) and the number of active sites per unit surface area of INPs (n_s) were measured under mixed-phase cloud conditions. The freezing experiments were continued until all droplets were frozen, but because most samples were already fully or nearly fully frozen by about −25 °C, the INP data presented and discussed in this study mainly span the temperature range from about −25 to −5 °C. Source apportionment of $PM_{2.5}$ using a positive matrix factorization (PMF) model enabled the identification of major emission sources and their temporal variations.

2 Methods

2.1 Sampling

Taiyuan is a major industrial city in northern China, often experiencing elevated concentrations and enrichment factors (EFs) of $PM_{2.5}$-bound heavy metals, influenced by local emissions, regional transport, and complex terrain (Li et al., 2021). A winter observation campaign was conducted from 3 December 2023 to 14 January 2024, coinciding with the centralized heating season characterized by intensive coal combustion. The sampling site (37.88° N, 112.55° E; approx-

imately 800 m a.s.l.) is located on the rooftop (~ 20 m above ground level) of a four-story building at the Taiyuan Municipal Ecology and Environment Bureau. Situated near Taoyuan 3rd Alley, this site is representative of a typical central urban environment. Although it is removed from direct major industrial point sources, it remains suitable for monitoring urban fine particulate pollution driven by mixed anthropogenic activities.

Key atmospheric pollutants were continuously monitored at the station, including concentrations of water-soluble ions, heavy metals, elemental carbon (EC) and organic carbon (OC), gas concentrations (SO_2, NO_x, O_3, CO), particulate matter concentrations ($PM_{2.5}$ and PM_{10}), together with meteorological parameters (wind speed, wind direction, temperature, relative humidity, and atmospheric pressure). In addition, INP filter samples were collected using a two-channel sampler equipped with two parallel filter channels from 4 December 2023 to 5 January 2024. Polycarbonate filters (47 mm, Nuclepore Track-Etch Membrane, 0.2 µm pore size, Whatman) were used for sampling. The sampler was operated without a size-selective inlet. The sampling flow rate was maintained at 6 L min^{-1} by a mass flow controller (MFC), with a 24 h sampling duration. Considering flow fluctuations and filter switching time, the total sampled air volume for each filter was approximately 8000 L. Except for the filter samples, all observation data were recorded as hourly averages.

2.2 Instrumentation

2.2.1 Particle mass and size distribution measurement

Mass concentrations of particulate matter (PM) with aerodynamic diameter (d_a) smaller than 2.5 and 10 µm ($PM_{2.5}$ and PM_{10}, respectively) were measured by a tapered element oscillating microbalance (TEOM) monitor.

Two scanning mobility particle sizer (SMPS) systems were employed to measure particle number size distributions in the 2.02–514 nm range during the campaign, while the range of data used in this study was 3–453 nm. The first system consisted of a TSI Classifier 3080 with Differential Mobility Analyzer (DMA) 3085 and Condensation Particle Counter (CPC) 3776, while the second system included a TSI Classifier 3082 with DMA 3081 and CPC 3772. Sample humidity was regulated using a Nafion™ membrane dryer (Perma Pure, MD-700-24F-3) to prevent water vapor condensation. Multiple charging corrections were applied during data processing (Wiedensohler, 1988).

An Optical Particle Counter (Aerosol Spectrometer and Dust Monitor 1.108, Grimm Aerosol Technik) was used to obtain the particle number size distribution (PNSD) of particles ranging from 0.5 to 20 µm in optical-equivalent diameters. To merge the OPC data with the SMPS measurements and calculate particle surface area on the same diameter basis, the OPC size distribution was converted to mobility diameter (d_m). Estimating d_a from optical-equivalent diameter typically requires knowledge of particle complex refractive index and morphological parameters (e.g., dynamic shape factor) (Peters et al., 2006). Moreover, when converting to dm, we assumed an effective particle density of 1.5 g cm^{-3} and a shape factor of unity. Previous sensitivity calculations showed that changing the particle density from 1.5 to 2.6 g cm^{-3} and the dynamic shape factor from 1.1 to 1.4 can lead to a factor of 1.07–2.36 difference in n_s (Chen et al., 2021). This suggests that diameter conversion may introduce an uncertainty of approximately a factor of 2 in n_s, particularly in the coarse-mode size range (Huang et al., 2021). A more exact uncertainty could not be assigned because particle refractive index, morphology, and particle-specific effective density were not independently measured. The OPC data were combined with the SMPS measurements to construct a merged particle size distribution (SMPS: 3–453 nm; OPC: 0.5–20 µm), which was further used to estimate the total particle surface area for n_s calculation.

2.2.2 Particle chemical composition

The water-soluble inorganic ions in $PM_{2.5}$ were measured in-situ using a Monitor for AeRosols and Gases in ambient Air (MARGA 1S; Metrohm AG, Switzerland). The analysis focused on major inorganic ions, including NO_3^-, SO_4^{2-}, NH_4^+, Cl^-, K^+, Ca^{2+}, Na^+ and Mg^{2+}. In parallel, the MARGA simultaneously measured the gaseous pollutants including SO_2, HNO_2, HNO_3, NH_3, and HCl. EC and OC concentrations were determined using a Carbonaceous Aerosol Speciation System (CASS; Aerosol d.o.o., Slovenia, EU) (Rumsey et al., 2014; Rumsey and Walker, 2016; Wan et al., 2022), following the thermal–optical transmittance method. Elemental composition of aerosol samples was analyzed by online X-ray fluorescence spectrometry (XRF) (Marguí et al., 2022), allowing quantification of a wide range of elements including light metals (K, Ca, etc.), metalloids (As, Se, etc.), and heavy metals (Zn, Pb, Cu, Hg, etc.).

2.2.3 Ice-nucleating particle (INP) concentration

N_{INP} concentrations were determined using the Peking University Ice Nucleation Array (PKU-INA), a cold-stage-based ice nucleation instrument (Chen et al., 2018, 2021). Each filter was fully immersed in 20 mL of double-distilled water (resistivity: 18.2 MΩ cm at 25 °C), and extracted using an ultrasonic shaker for 30 min. Ultrasonic extraction is an effective method for removing particles from filters (Ardon-Dryer and Levin, 2014; Chen et al., 2018; Reicher et al., 2019; Chen et al., 2021), although it may alter the bioactivity of proteins (De Leo et al., 2017). To minimize ultrasound-induced heating, the extraction was performed in a water bath with ice. The resulting suspension was dispensed into 90 droplets (1 µL each) on a hydrophobic glass slide. A metal spacer was placed on the slide to assist in droplet positioning and

to suppress the Wegener–Bergeron–Findeisen process (Jung et al., 2012). A top glass was placed on the spacer to seal the droplets. The cold stage was first cooled from room temperature to 0 °C at 20 °C min^{-1}, and then at 1 °C min^{-1} until all droplets were frozen. The image of each droplet was recorded by a CCD camera every 6 s, corresponding to a temperature resolution of 0.1 °C. These images were later analyzed by customized software to identify the phase transition of each droplet by its brightness change upon freezing. High-purity dry nitrogen was used as sheath gas to prevent condensation and frost formation. The temperature uncertainty at the applied cooling rate was within ±0.4 °C (Chen et al., 2018).

The cumulative number of ice-active sites per unit droplet volume above temperature T was calculated according to Vali et al. (2015):

$$K(T) = -\frac{\ln(1 - f_{\mathrm{ice}}(T))}{V} \quad (\mathrm{cm}^{-3} \text{ of water}) \tag{1}$$

where $f_{\mathrm{ice}}(T)$ is the fraction of droplets frozen at T, and V is the volume of each pipetted droplet (1 µL in this study). Combined with the total sampling volume, the $N_{\mathrm{INP}}(T)$ per unit volume of sampled air is calculated as

$$N_{\mathrm{INP}}(T) = -\frac{\ln(1 - f_{\mathrm{ice}}(T))}{V_{\mathrm{air}}} \quad (\mathrm{L}^{-1} \text{ air}) \tag{2}$$

where V_{air} is the total volume of sampled air per droplet converted to standard conditions (0 °C, 1013 hPa) during each sample collection period. To quantify and compare the ice-nucleating activity of aerosol particles of different sizes, the n_{s} (Vali et al., 2015), i.e., the cumulative ice-nucleation-active-site surface density (Connolly et al., 2009; Niedermeier et al., 2011; Hoose and Möhler, 2012), is calculated from the $N_{\mathrm{INP}}(T)$ as

$$n_{\mathrm{s}}(T) = \frac{N_{\mathrm{INP}}(T)}{A} \quad (\mathrm{m}^{-2}) \tag{3}$$

where A is the total surface area of the particles per unit volume of sampled air, derived from size distribution measurements of the particles. For $n_{\mathrm{s}}(T)$ calculation, the merged SMPS–OPC particle number size distributions were converted to the same standard-condition air-volume basis as N_{INP} (0 °C, 1013 hPa) using concurrent temperature and pressure data. The particle surface area was then estimated from the converted size distributions expressed in mobility diameter.

The main source of uncertainty in the experimental results stems from the statistical representativeness of the droplets analyzed relative to the entire particle suspension. Due to the low ambient concentrations of INPs, the number of INPs present in the resulting particle suspension is typically small. As each droplet has a volume of only 1 µL, individual droplets may not adequately reflect the true particle distribution in the bulk extract. Moreover, the total number of droplets tested per sample (90 in this study) imposes a statistical limitation. To account for this, confidence intervals for the estimated INP concentration per droplet (and per unit sample volume) were calculated following the statistical approach described in previous studies (Barker, 2002; O'Sullivan et al., 2018), as shown in Eq. (4):

$$\mu(T) + \frac{(Z_{\alpha/2})^2}{2n} \pm Z_{\alpha/2}\left[4\mu + \frac{(Z_{\alpha/2})^2}{n}\right]^{0.5} \Big/ (4n)^{0.5} \tag{4}$$

where $\mu(T)$ represents the number of INPs per droplet, n is the total number of droplets analyzed, and $Z_{\alpha/2}$ denotes the standard normal score corresponding to the desired confidence level (1.96 for a 95 % confidence interval).

For each aerosol sample, the parameters ($f_{\mathrm{ice}}(T)$, $K(T)$, $N_{\mathrm{INP}}(T)$, $n_{\mathrm{s}}(T)$, and the confidence intervals for $N_{\mathrm{INP}}(T)$) were calculated individually. The $f_{\mathrm{ice}}(T)$ was derived from cold-stage measurements, V_{air} was obtained from recorded sampling volumes, and A was calculated from the standard-condition combined particle size distributions measured by the SMPS and OPC. The uncertainty in ns arises from both the statistical uncertainty in N_{INP} and the uncertainty in the particle surface area concentration used for normalization. The latter is mainly associated with the SMPS–OPC merging and diameter conversion in the coarse-mode range, as discussed in Sect. 2.2.1.

2.2.4 Air mass backward trajectory analysis

Backward trajectory analysis and visualization were performed using the MeteoInfoMap program (Wang, 2014), which is based on the HYSPLIT4 (Hybrid Single-Particle Lagrangian Integrated Trajectory) model developed by the NOAA (National Oceanic and Atmospheric Administration, USA) Air Resources Laboratory. The analysis used GDAS (Global Data Assimilation System, 1°, global) meteorological data from NOAA (Stein et al., 2015). Trajectories were calculated with a duration of 72 h and an interval of 6 h between each trajectory, arriving at an altitude of 850 m above sea level (a.s.l.), which approximately represents the actual sampling inlet height, considering a ground elevation of about 800 m a.s.l. and a rooftop sampling height of about 20 m above ground level.

2.2.5 Positive matrix factorization (PMF)

The Positive Matrix Factorization (PMF) model was applied to analyze the sources of $PM_{2.5}$. PMF is a widely used receptor model for source apportionment. It can identify the composition and contribution of various sources. The model assumes that species emitted from the same source exhibit strong correlations, enabling the extraction of meaningful factors from measured concentration data (Karagulian et al., 2015; US EPA, 2015).

Given an $m \times n$ matrix $\mathbf{X}$ consisting of concentrations of n chemical species across m samples, PMF decomposes the matrix into two positive matrices – factor contributions ($\mathbf{G}$)

and factor profiles (**F**) – according to Eq. (5):

$$\boldsymbol{X}_{ij} = \sum_{k=1}^{p} \boldsymbol{G}_{ik}\boldsymbol{F}_{kj} + \boldsymbol{E}_{ij} \tag{5}$$

where p is the number of factors, i denotes the sample index, and j represents the species index. $\boldsymbol{X}_{ij}$ is the measured concentration of species j in sample i; $\boldsymbol{G}_{ik}$ represents the contribution of factor k to sample i; $\boldsymbol{F}_{kj}$ is the mass fraction of species j in factor k; and $\boldsymbol{E}_{ij}$ denotes the residuals. Both $\boldsymbol{G}_{ik}$ and $\boldsymbol{F}_{kj}$ are constrained to be non-negative.

To obtain the optimal solution, PMF minimizes an objective function Q (Eq. 6) using uncertainty estimates u_{ij} and non-negativity constraints on $\boldsymbol{G}$ and $\boldsymbol{F}$:

$$Q = \sum_{i=1}^{m}\sum_{j=1}^{n}\left(\frac{\boldsymbol{X}_{ij} - \sum_{k=1}^{p}\boldsymbol{G}_{ik}\boldsymbol{F}_{kj}}{u_{ij}}\right)^2 \tag{6}$$

The uncertainty u_{ij} is estimated following the EPA PMF 5.0 User Guide (US EPA, 2015) as:

$$u_{ij} = \begin{cases} \frac{5}{6} \times \mathrm{MDL} & (c \le \mathrm{MDL}) \\ \sqrt{(\mathrm{ef} \times \boldsymbol{X}_{ij})^2 + (0.5 \times \mathrm{MDL})^2} & (c > \mathrm{MDL}) \end{cases} \tag{7}$$

where c is the measured concentration of a given species, MDL is the method detection limit, and ef is the analytical uncertainty, typically between 0.05 and 0.2. In this study, ef = 0.1 was applied.

EPA PMF 5.0 software was employed for source apportionment of $PM_{2.5}$ in the study region. The specific datasets and their sources used for PMF analysis are described in Sect. 3.4. To determine the optimal number of factors, 4–7 factors were tested with 20 iterative runs each, and the solution with the most physically interpretable source profiles and lowest residuals was selected for final analysis (US EPA, 2015). Consequently, a five-factor solution was determined to be the optimal choice.

3 Results and discussion

3.1 Overview of INP temporal variability and aerosol characteristics

Figure 1 presents the temporal evolution of atmospheric INP concentrations and relevant aerosol parameters during the observation period in Taiyuan, including size-segregated particle number concentrations, carbonaceous components (OC and EC), as well as mass concentrations of $PM_{2.5}$ and PM_{10}, and water-soluble ions. Daily N_{INP} at different temperatures are shown in Fig. 1a (data for 15, 16, and 19 December are missing). At and above −15 °C, the cumulative $N_{INP}(T)$, representing the total INP concentration active at and above this temperature, ranged from 10^{-2} to 10^{1} L^{-1} with a campaign mean of 1.75 L^{-1}. The corresponding 95 % confidence intervals for N_{INP} at selected temperatures are provided in Table S3 in the Supplement. Correspondingly, the n_s values at and above −15 °C (see Fig. 3) spanned 10^5 to 10^7 m^{-2}, with a campaign mean of 3.42×10^6 m^{-2}.

Several distinct events can be identified throughout the campaign, as highlighted in Fig. 1 by dashed boundary lines and colored arrows. The first event (5–9 December, marked by the orange arrow in Fig. 1a) was characterized by a sharp increase in coarse-mode particle concentrations, represented here by $N_{>1\,\mu m}$ derived from the merged SMPS–OPC size distribution (Figs. 1b, S1b, and S2 in the Supplement). During this episode, the mean $N_{>1\,\mu m}$ increased to 5.94 cm^{-3}, which was approximately 2.7 times higher than the average concentration during the remaining observation periods (2.21 cm^{-3}). A peak daily concentration of 12.08 cm^{-3} was recorded on 6 December, accompanied by a steep rise in PM_{10} that reached nearly 800 $\mu g\,m^{-3}$ (Fig. 1b and d).

72 h back trajectory analysis by HYSPLIT model confirmed that air masses during this period predominantly originated from the Taklamakan, Gurbantünggüt, or Badain Jaran Deserts in northwestern China, with trajectory paths highly overlapping the desert regions (Fig. S3 in the Supplement). This pattern is consistent with desert dust transport events previously observed in northern China (Chen et al., 2021), further supporting the identification of this period as a desert dust intrusion event. Wind rose analysis (Fig. S6 in the Supplement) shows that both the dust-event and non-desert-dust periods were dominated by northerly flow, whereas the dust-event period exhibited a more concentrated northerly flow pattern. This serves as supplementary meteorological support for the event classification. Given the well-established high ice-nucleating activity of mineral dust, this episode is identified as a desert dust-intrusion event responsible for the pronounced enhancement in N_{INP}, especially at temperatures > −12.5 °C. The remaining observation periods are not assumed to be free of mineral dust influence; rather, no similarly clear desert dust intrusion signature was identified outside this event. Further discussion of its characteristics and implications is provided in Sect. 3.2.

Other episodes (13–14, 18, and 28–30 December, marked by the gray arrows in Fig. 1a) were characterized by simultaneous increases in sulfate, nitrate, ammonium, and organic carbon, accompanied by elevated $PM_{2.5}$ and PM_{10} levels (Fig. 1c and d). This indicates the influence of air pollution driven by regional secondary aerosol accumulation under stagnant winter meteorology. Moderate N_{INP} increases were observed during the earlier two episodes (13–14 and 18 December), suggesting that secondary aerosol formation may indirectly modulate ice-nucleating activity through coating or mixing with pre-existing ice-active particles. The late-December event showed no corresponding N_{INP} enhancement despite high PM levels, indicating that aerosol mass concentration alone may not determine INP abundance. This contrast emphasizes that particle composition and surface properties, rather than overall pollution intensity, govern INP

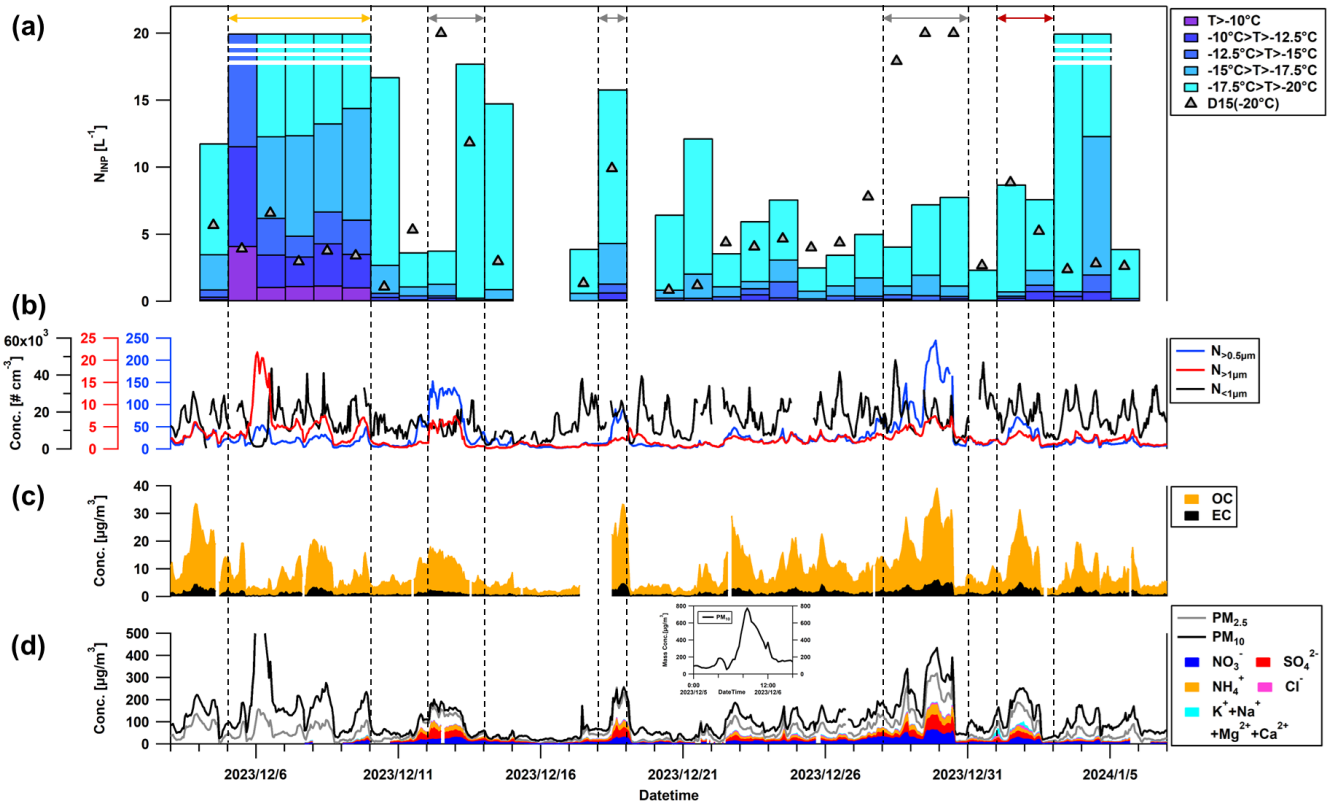

Figure 1. Time series of **(a)** temperature-resolved N_{INP}, **(b)** size-resolved particle number concentrations, **(c)** mass concentrations of OC and EC, and **(d)** mass concentrations of $PM_{2.5}$, PM_{10} and major water-soluble ions (K^+, Na^+, Mg^{2+}, Ca^{2+}, Cl^-, NH_4^+, SO_4^{2-}, NO_3^-) measured by MARGA during the observation period. In panel **(a)**, gray triangles (D15(−20 °C)) represent values calculated using the parameterization of DeMott et al. (2015), shown here mainly as a dust-based reference for comparison with the observed day-to-day temporal variation in INP concentrations. Special periods are indicated by dashed boundary lines across all panels and colored arrows at the top of panel **(a)**: the orange arrow denotes the desert dust period, the gray arrows denote pollution periods, and the red arrow denotes the fireworks event. In panel **(a)**, white horizontal lines indicate samples for which all droplets had already frozen before the colder temperature intervals were reached. Under these conditions, the cumulative N_{INP} exceeded the quantifiable range of the assay and therefore could not be plotted as a finite value. In panel **(b)**, $N_{<1\,\mu m}$ refers to particles from 3 nm to 1 µm, whereas $N_{>0.5\,\mu m}$ and $N_{>1\,\mu m}$ denote the concentrations integrated over 0.5–20 µm and 1–20 µm, respectively. The inset in panel **(d)** shows the full PM_{10} peak on 5–6 December. Ion data before approximately 7 December 2023 were unavailable and are therefore not shown in panel **(d)**.

activity during pollution episodes characterized by enhanced secondary inorganic and organic aerosol accumulation (Chen et al., 2018; Wagh et al., 2021; Zhang et al., 2022).

Around 2 January 2024 (marked by the red arrow in Fig. 1a), a short-lived pollution event occurred, accompanied by sharp increases in PM mass and concurrent peaks in K, OC, EC (Fig. 1c and d), which are consistent with firework emissions during New Year celebrations. Despite elevated particle concentrations and combustion-related aerosol components, N_{INP} remained low, suggesting that freshly emitted anthropogenic particles, including black carbon and other combustion products, are relatively inefficient as INPs, consistent with previous observations that even locally high concentrations of combustion aerosols contribute little to atmospheric ice-nucleating activity (Adams et al., 2020; Zhang et al., 2022).

3.2 Comparison with previous urban studies and parameterizations

Figure 2 compares the measured N_{INP} in this study with values reported previously. All samples in Taiyuan activated before −15 °C, with the most active samples initiating freezing near −5 °C. The N_{INP} varied by more than two orders of magnitude among different samples, particularly in the −10 to −15 °C range, where values ranged from below 0.01 L^{-1} to above 10 L^{-1}. Such variability primarily reflects the influence of the desert dust intrusion identified earlier (highlighted in darker orange in Fig. 2), during which enhanced N_{INP} values were observed due to long-range transport of natural mineral particles. However, the enhanced warm-temperature INP activity during this episode may not be fully attributable to mineral dust alone. During East Asian dust events, Chen et al. (2021) showed that heat-

sensitive INPs made substantial contributions at relatively warm temperatures. Similarly, Hu et al. (2023) reported enhanced warm-temperature INP activity during spring dust transport in Beijing and suggested, based on heat-treatment analysis, that transported dust particles may be mixed with heat-sensitive, potentially biological components. Together, these studies support the possibility of similar heat-sensitive contributions during the Taiyuan dust episode. In the present study, however, no heat-treatment analysis was performed; therefore, such a contribution can only be inferred and cannot be directly assessed.

For the remaining non-desert-dust periods, N_{INP} in Taiyuan was generally higher than wintertime urban observations in Beijing measured by INDA (Chen et al., 2018) and in Tokyo (Tobo et al., 2020) over much of the overlapping temperature range. This difference may be related to the semi-arid setting of Taiyuan and its proximity to the Loess Plateau and northwestern dust source regions, where mineral and resuspended dust particles can provide a more persistent background of coarse-mode aerosol than in the Beijing and Tokyo observations. Consistently, particles larger than 1 µm remained at appreciable concentrations even outside the identified desert dust event, although no clear desert-dust intrusion signature comparable to the 5–9 December episode was identified. Differences in sampling size range should also be considered, because the Taiyuan INP filters were collected without a size-selective inlet and can be regarded as approximately total suspended particles (TSP), whereas Chen et al. (2018) collected $PM_{2.5}$ samples in Beijing. The anthropogenic-dust samples collected in Beijing in summer (Chen et al., 2024) overlap mainly with the lower part of the Taiyuan data. These comparisons suggest the higher Taiyuan N_{INP} levels likely reflect a combination of regional dust influence, local dust-associated coarse particles, seasonal differences, and sampling-size-range differences, rather than a single controlling factor.

The linear N_{INP} parameterizations derived from field measurements in Beijing (Bi et al., 2018) and Huangshan (Su et al., 2014) also capture the overall magnitude of the present measurements. Additionally, the gray shaded area denotes the N_{INP} range derived from precipitation samples summarized by Petters and Wright (2015), which is used here as a broad reference for background atmospheric INP abundance. At temperatures warmer than −15 °C, the Taiyuan N_{INP} values fall mostly within this range during the non-desert-dust periods. At colder temperatures, however, the measured N_{INP} values exceed this range substantially, suggesting contributions from additional ice-active components active at lower temperatures. Taken together, these features indicate that episodic desert dust transport was associated with the most prominent INP enhancements during this campaign, whereas the remaining variability during the non-desert-dust periods likely reflects a more complex mixture of sources and particle properties that cannot be uniquely resolved by the present dataset.

3.3 Characterization of dust INPs

During the desert dust event (5–9 December; marked by the orange arrow and dashed boundary lines in Fig. 1a), both N_{INP} and n_s increased markedly. At and above −15 °C, N_{INP} reached 13.37 L^{-1} and n_s peaked at 3.11×10^7 m^{-2}, while their mean values rose from 0.61 to 7.47 L^{-1} and from 9.52×10^5 to 1.57×10^7 m^{-2}, respectively. These coherent increases in concentration and surface-active-site density indicate that the episode was characterized by both an increased abundance of INPs and substantially enhanced intrinsic ice-nucleating activity. The n_s values discussed here were calculated from the standard-condition merged SMPS–OPC size distribution, thereby accounting for contributions from coarse particles in the surface-area estimate. Figure 1a also compares the measurements with the DeMott et al. (2015) parameterization (D15), which links INP concentrations to the number concentration of particles larger than 0.5 µm and was originally developed for desert dust aerosol. In this study, the D15 values were calculated using the observed particle number concentrations larger than 0.5 µm and are therefore shown mainly as a dust-based reference. Accordingly, the comparison is most meaningful for the identified dust episode, whereas for the remaining periods it should be interpreted with caution. While D15 captures the correct order of magnitude, it tends to underestimate the INP peak during the desert dust event (5–9 December) and overestimate INP concentrations during the pollution episode (28–30 December). This discrepancy suggests that coarse-particle abundance alone may not fully constrain INP variability in Taiyuan. Particles larger than 0.5 µm in Taiyuan outside the identified desert dust event may differ in source characteristics and ice-nucleating efficiency from those of the highly active desert dust represented by the D15 parameterization. The apparent overestimation by D15 during pollution episodes implies that these coarse particles may possess lower ice-nucleating efficiency than the highly active desert dusts represented by the parameterization. Therefore, while size-based parameterizations provide a useful approximation, incorporating source-specific or compositional factors could further improve INP predictability in such complex industrial-urban environments.

Figure 3 compares n_s as a function of temperature for desert dust-affected samples (red) with non-desert-dust samples (blue). Across the full temperature range, dust-affected samples exhibit systematically higher n_s values than non-desert-dust samples. Between −10 and −15 °C, desert dust-affected samples exhibited n_s values approximately one order of magnitude higher than the most active non-desert-dust samples. In the colder range (−20 to −15 °C), most dust-affected samples fall within about one order of magnitude of the desert-dust parameterizations proposed by Niemand et al. (2012) and Chen et al. (2021), indicating ice-nucleating behavior consistent with long-range transported mineral dust. Considering that Taiyuan is located on the western edge of

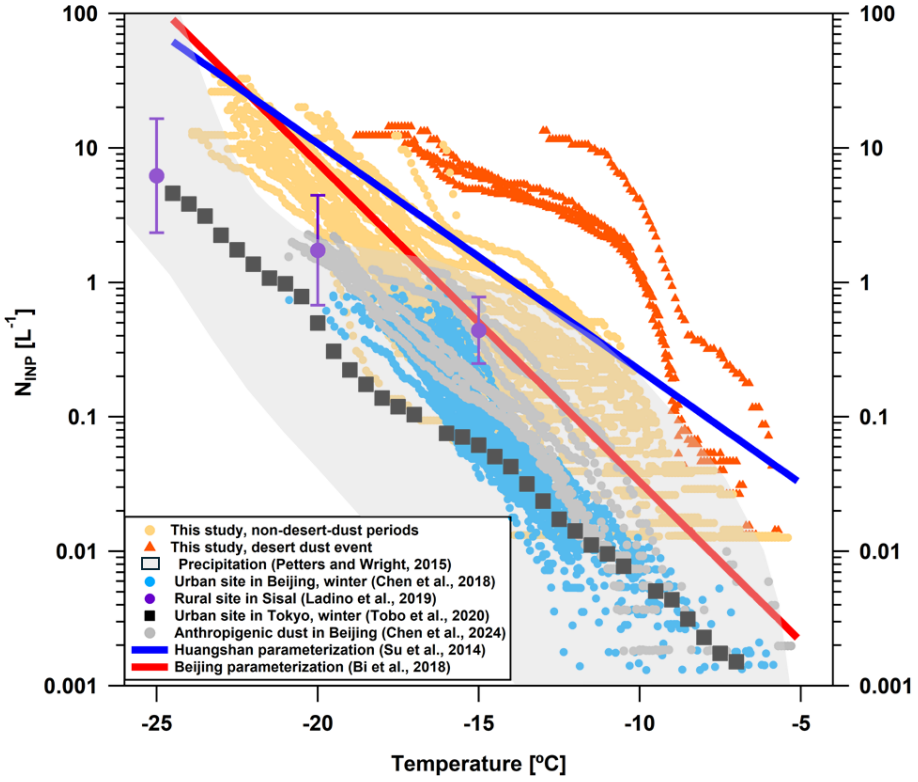

Figure 2. Comparison of N_{INP} obtained in this study with those reported in previous studies. Pale-yellow circles represent N_{INP} values from this study during non-desert-dust periods, while orange triangles denote data collected during the identified desert dust event. Blue circles denote wintertime urban INP observations in Beijing measured by INDA during November–December 2016 (Chen et al., 2018), and black squares denote wintertime urban INP observations in Tokyo during December 2016–February 2017 (Tobo et al., 2020). Purple circles indicate data from Sisal, Mexico (Ladino et al., 2019), and gray circles show anthropogenic-dust samples collected in Beijing (Chen et al., 2024). Solid red and blue lines correspond to parameterizations for Beijing and Huangshan (Bi et al., 2018; Su et al., 2014). The light-gray shaded area shows N_{INP} ranges from precipitation samples (Petters and Wright, 2015).

the North China Plain while Beijing lies farther downwind, dust arriving in Beijing may have experienced a longer transport history and more atmospheric processing. As shown in Fig. 3, the Beijing dust parameterization broadly overlaps with the ns values of the dust samples in this study across the measured temperature range. This comparison is consistent with Chen et al. (2023), who reported observational evidence that atmospheric chemical modification did not suppress the ice nucleation activity of East Asian dust. However, because the present study did not directly characterize the aging state of the dust particles or the specific aging processes involved, this comparison is used only to suggest that strong ice-nucleating activity was retained during the Taiyuan dust episode, rather than to demonstrate or quantify the effect of atmospheric aging.

It is also noteworthy that at relatively warm temperatures (approximately $T > -12\,^{\circ}\mathrm{C}$), n_s values of the ambient desert dust samples substantially exceed the parameterizations for pure K-feldspar (Atkinson et al., 2013; Harrison et al., 2019), suggesting that mineralogy alone cannot account for the elevated warm-temperature activity. Previous laboratory and field studies have shown that mineral dust particles can act synergistically with biological macromolecules or cellular fragments, leading to pronounced enhancement of heterogeneous freezing at warmer temperatures (Augustin-Bauditz et al., 2016; O'Sullivan et al., 2016; Yahya et al., 2019). The enhanced n_s observed at $T > -12\,^{\circ}\mathrm{C}$ in this study may therefore reflect the combined influence of mineral dust and potentially co-transported biological INP components, rather than mineral dust alone. The TSP-like sampling configuration may have facilitated retention of such coarse ice-active components, but it cannot by itself explain the selective enhancement observed during the dust event.

3.4 Anthropogenic particle pollution and INP variability during non-desert-dust periods

The Pearson correlation coefficients between N_{INP} at different temperatures and various pollutants were calculated for non-desert-dust periods. As shown in Table S1 in the Supplement, only Ca, Co, Ni, and Au exhibited statistically significant correlations ($p < 0.05$; $n = 24$). The mean concen-

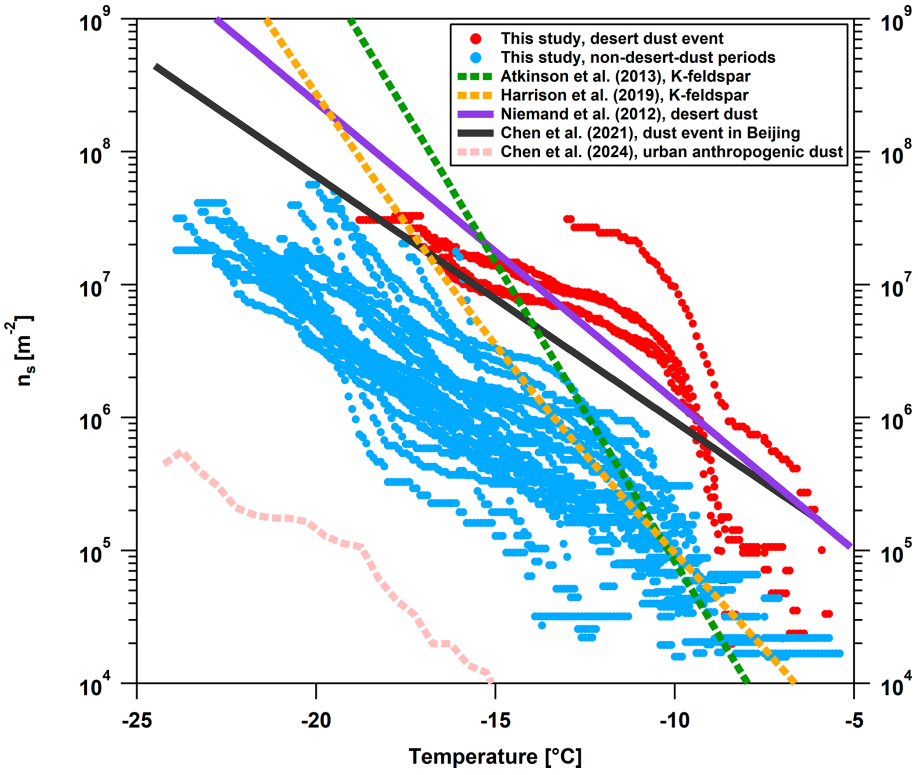

Figure 3. Comparison of n_s obtained in this study with those reported in previous studies. Blue and red markers represent the n_s values of samples from this study during non-desert-dust periods and the identified desert dust event, respectively. The lines show n_s parameterizations for dust or individual mineral components reported in previous studies (Atkinson et al., 2013; Chen et al., 2021; Harrison et al., 2019; Niemand et al., 2012). The light-pink dashed line denotes the median trend of n_s values for urban anthropogenic dust particles in Beijing, digitized from Chen et al. (2024).

trations of Co, Ni, and Au were all below 10 ng m^{-3}, suggesting that their correlations are of limited physical relevance. By contrast, Ca averaged about 405 ng m^{-3} but was notably correlated only with N_{INP} at −10 °C. As a typical crustal element, Ca is closely linked to particles larger than 1 µm (Chen et al., 2024). Excluding the influence of long-range dust transport, this observation likely points to contributions from local or regional dust-associated particles, such as resuspended soil and fugitive dust.

The weak correlations for all pollutants highlight that individual chemical species provide limited explanatory power for INP variability during non-desert-dust periods. This reflects the fact that INPs constitute only a minor and compositionally distinct subset of the total aerosol population, and thus bulk pollutant concentrations are not expected to correlate strongly with N_{INP}. To further examine whether the dominant $PM_{2.5}$ source factors were associated with N_{INP} variability during the non-desert-dust periods, PMF analysis was applied to the $PM_{2.5}$ chemical composition dataset, resolving five major factors (industry, dust-related particles, secondary aerosols, coal combustion and traffic, and fireworks). The corresponding factor profiles (Fig. S4 in the Supplement) are consistent with the assigned source categories, including crustal tracers in the dust-related factor and Cu–Ba–K enrichment in the fireworks factor. The inter-species correlation patterns shown in Fig. S5 in the Supplement also support these factor assignments. Because the PMF analysis was based on $PM_{2.5}$ whereas the INP filter samples can be regarded as approximately TSP, the PMF results are used here only to assess covariation with N_{INP}, rather than to provide direct source apportionment for INPs. Data from the identified desert dust event (5–9 December) are not shown in Fig. 4, because the PMF–N_{INP} correlation analysis focused on non-desert-dust periods. The dust-related factor exhibits characteristic signatures of dust-associated particles, including high loadings of Ca and Fe. During the non-desert-dust periods, this factor is interpreted as mainly reflecting local dust-associated particles, such as road dust, fugitive dust from industrial and construction activities, and resuspended soil. This dust-related $PM_{2.5}$ factor showed no significant correlation with N_{INP} during the non-desert-dust periods (Table 1), indicating that local dust-associated $PM_{2.5}$ variability did not explain N_{INP} variability outside the identified long-range desert dust event. The reconstructed daily $PM_{2.5}$ contributions (Fig. 4) provide the temporal context for the subsequent PMF–N_{INP} correlation analysis, showing

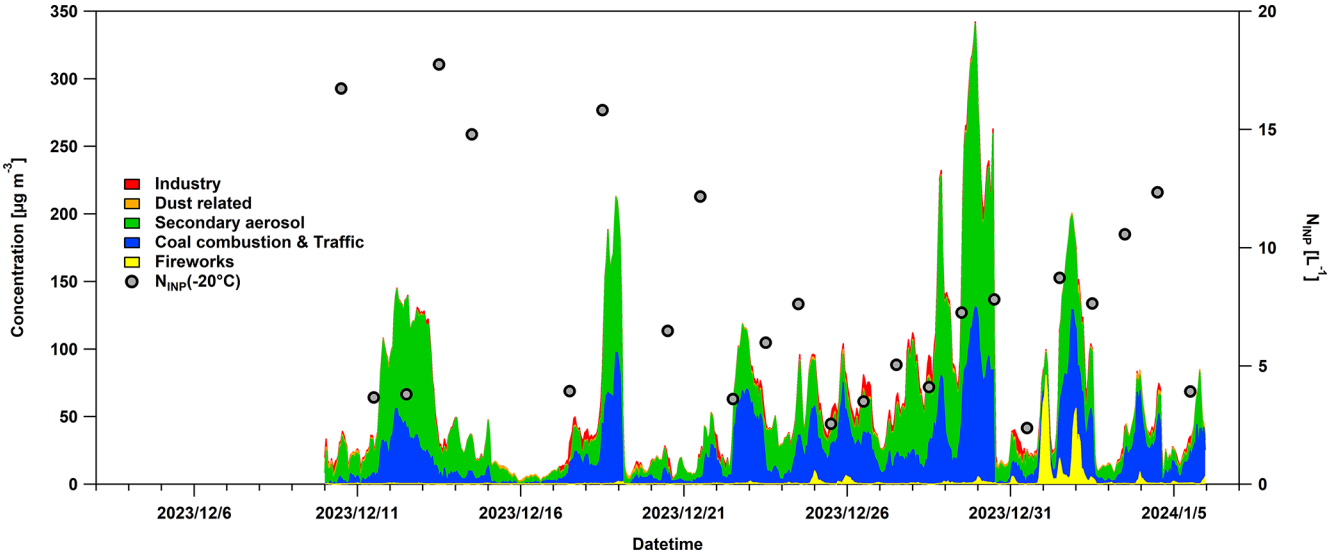

Figure 4. Daily $PM_{2.5}$ source contributions resolved using the PMF model, shown together with the corresponding N_{INP} at −20 °C during the non-desert-dust periods. Data from the identified desert dust event are not shown. The samples collected on 13, 14, 21 December and 3, 4 January were fully frozen before −20 °C, exceeding the quantifiable range of the assay.

Table 1. Pearson correlation coefficients (r) and corresponding p values between N_{INP}(−20 °C) and concentration contributions of PMF-resolved factors during non-desert-dust periods.

Aerosol Source	Pearson r value	p value
Industry	−0.264	0.274
Dust related	0.209	0.391
Secondary aerosol	0.145	0.554
Coal & Traffic	0.035	0.886
Fireworks	0.108	0.661

that secondary aerosols and coal/traffic emissions dominated the $PM_{2.5}$ mass during much of the non-desert-dust period, whereas fireworks emissions became prominent during the New Year period.

To evaluate whether any of these major $PM_{2.5}$ sources covaried with INP, Pearson correlations were calculated between N_{INP} at −20 °C and the time series of the PMF factors during non-desert-dust periods (Table 1). All correlations were weak ($|r| < 0.3$) and statistically insignificant ($p > 0.05$), indicating that the dominant $PM_{2.5}$ source factors did not show clear covariation with INP abundance. Importantly, even during periods with strong increases in secondary inorganic and organic aerosols, such as 13–14 December, 18 December, and 28–30 December, N_{INP} did not rise proportionally (Fig. 4). This behavior suggests that the observed pollution episodes, which were largely associated with fine-mode secondary aerosol accumulation, were not accompanied by corresponding INP enhancements, consistent with previous urban observations showing weak relationships between INPs and bulk pollution indicators (Chen et al., 2018; Zhang et al., 2022).

These results suggest that, during non-desert-dust periods of this campaign, N_{INP} variability was not clearly explained by any of the major PMF-resolved source categories. This is consistent with previous observations at urban sites in different regions, where INPs remain scarce and episodic relative to total aerosol loading, and where their variability is often not well explained by the major anthropogenic aerosol components. Similar analyses were also conducted at −10, −12.5, −15, and −17.5 °C (Table S2 in the Supplement). No statistically significant correlations were found between N_{INP} and any PMF-resolved factor at the examined temperatures ($p > 0.05$), indicating that this result was not specific to the choice of −20 °C.

4 Conclusions

This study provides a detailed observational assessment of atmospheric INPs in Taiyuan, a heavily industrialized city in North China. By combining freezing assays, aerosol chemical composition, back-trajectory analysis, and PMF analysis, the work characterizes the concentration range, temperature dependence of INP activation, and variability of INPs in an urban environment where such information has been largely absent. The results provide observational constraints on wintertime INP abundance and variability in an industrial urban atmosphere.

A key finding of this winter campaign is that the strongest INP enhancements in Taiyuan were associated with episodic long-range desert dust transport. During the 5–9 December desert dust event, N_{INP} and ns increased by up to an or-

der of magnitude and freezing initiated at markedly warmer temperatures. Back trajectories confirmed that these highly active samples were associated with air masses originating from the major desert regions in northwestern China. Comparison with previously reported dust parameterizations indicates that the transported desert dust retained strong ice-nucleating activity during the dust transport episode. The enhanced warm-temperature activity may also reflect the possible contribution of co-transported biological components, although this cannot be directly verified in the absence of heat-treatment analysis.

In contrast, during the non-desert-dust periods of this campaign, N_{INP} remained relatively low and showed weak correlations with common urban aerosol species. PMF analysis resolved five major $PM_{2.5}$ source factors: industrial emissions, dust-related particles, secondary aerosols, coal combustion and traffic emissions, and fireworks, with secondary aerosols and coal/traffic contributions dominating the particle mass. However, none of these PMF-resolved factors showed statistically significant covariation with N_{INP} during the non-desert-dust periods. This suggests that INP abundance during these periods could not be clearly explained by the dominant contributors to $PM_{2.5}$ mass.

Overall, the observations from this winter campaign indicate that the strongest INP enhancements in Taiyuan were associated with long-range desert dust transport, whereas the remaining INP variability during the non-desert-dust periods reflected more complex influences that were not resolved by the major $PM_{2.5}$ source factors considered here. These results provide observational constraints for understanding wintertime urban INPs and for improving their representation in chemical transport and climate models.

Data availability. The data supporting this study are available from Zenodo at https://doi.org/10.5281/zenodo.20232172 (Yang et al., 2026). The dataset includes INP freezing data, temperature-resolved NINP and confidence intervals, particle size distributions and surface area data, auxiliary observations, PMF source contribution data, and HYSPLIT backward trajectory outputs.

Supplement. The supplement related to this article is available online at https://doi.org/10.5194/acp-26-11771-2026-supplement.

Author contributions. JY, JingC and ZW designed experiments and methodology. JY, WF, JingC and ZF conducted the field observation. JY, ZW, WF, ZF, TZ, YQ, JunW and RM performed aerosol chemical and size distribution analyses; specifically, YQ was responsible for PMF (Positive Matrix Factorization) analysis, while JunW and RM assisted with offline sampling and chemical component analysis. JY, JieC and JingC calibrated the PKU-INA. TZ and WF provided meteorological data. MH, ZW, YL and NT supervised the study. JY, ZW, JieC and JingC prepared the article with input from all co-authors.

Competing interests. The contact author has declared that none of the authors has any competing interests.

Disclaimer. Publisher's note: Copernicus Publications remains neutral with regard to jurisdictional claims made in the text, published maps, institutional affiliations, or any other geographical representation in this paper. The authors bear the ultimate responsibility for providing appropriate place names. Views expressed in the text are those of the authors and do not necessarily reflect the views of the publisher.

Acknowledgements. We thank Ling Mu, Jiajie Li, Ying Wei, and Chenhui Li (Taiyuan University of Technology) for collecting the offline membrane samples.

Financial support. This research has been supported by the National Natural Science Foundation of China (grant no. 42375093), the Exploratory Innovation Project of the National Institute of Metrology, China (grant no. AKYCX2512), and the cooperative research programs of the Institute of Nature and Environmental Technology, Kanazawa University, Japan (grant nos. 25001 and 25015).

Review statement. This paper was edited by Daniel Knopf and reviewed by four anonymous referees.

References

Adams, M. P., Tarn, M. D., Sanchez-Marroquin, A., Porter, G. C. E., O'Sullivan, D., Harrison, A. D., Cui, Z., Vergara-Temprado, J., Carotenuto, F., Holden, M. A., Daily, M. I., Whale, T. F., Sikora, S. N. F., Burke, I. T., Shim, J.-U., McQuaid, J. B., and Murray, B. J.: A Major Combustion Aerosol Event Had a Negligible Impact on the Atmospheric Ice-Nucleating Particle Population, J. Geophys. Res.-Atmos., 125, e2020JD032938, https://doi.org/10.1029/2020JD032938, 2020.

Ansmann, A., Tesche, M., Althausen, D., Müller, D., Seifert, P., Freudenthaler, V., Heese, B., Wiegner, M., Pisani, G., Knippertz, P., and Dubovik, O.: Influence of Saharan dust on cloud glaciation in southern Morocco during the Saharan Mineral Dust Experiment, J. Geophys. Res.-Atmos., 113, D04210, https://doi.org/10.1029/2007JD008785, 2008.

Ardon-Dryer, K. and Levin, Z.: Ground-based measurements of immersion freezing in the eastern Mediterranean, Atmos. Chem. Phys., 14, 5217–5231, https://doi.org/10.5194/acp-14-5217-2014, 2014.

Atkinson, J. D., Murray, B. J., Woodhouse, M. T., Whale, T. F., Baustian, K. J., Carslaw, K. S., Dobbie, S., O'Sullivan, D., and Malkin, T. L.: The importance of feldspar for ice nucleation by mineral dust in mixed-phase clouds, Nature, 498, 355–358, https://doi.org/10.1038/nature12278, 2013.

Augustin-Bauditz, S., Wex, H., Kanter, S., Ebert, M., Niedermeier, D., Stolz, F., Prager, A., and Stratmann, F.: The immersion mode ice nucleation behavior of mineral dusts: A comparison of dif-

ferent pure and surface modified dusts, Geophys. Res. Lett., 41, 7375–7382, https://doi.org/10.1002/2014GL061317, 2014.

Augustin-Bauditz, S., Wex, H., Denjean, C., Hartmann, S., Schneider, J., Schmidt, S., Ebert, M., and Stratmann, F.: Laboratory-generated mixtures of mineral dust particles with biological substances: characterization of the particle mixing state and immersion freezing behavior, Atmos. Chem. Phys., 16, 5531–5543, https://doi.org/10.5194/acp-16-5531-2016, 2016.

Barker, L.: A Comparison of Nine Confidence Intervals for a Poisson Parameter When the Expected Number of Events is ≤ 5, Am. Stat., 56, 85–89, https://doi.org/10.1198/000313002317572736, 2002.

Bi, K., Ma, X., Chen, Y., Fu, S., and Xue, H.: The Observation of Ice-Nucleating Particles Active at Temperatures above–15 °C and Its Implication on Ice Formation in Clouds, J. Meteorol. Res.-PRC, 32, 734–743, https://doi.org/10.1007/s13351-018-7181-z, 2018.

Cabrera-Segoviano, D., Pereira, D. L., Rodriguez, C., Raga, G. B., Miranda, J., Alvarez-Ospina, H., and Ladino, L. A.: Inter-annual variability of ice nucleating particles in Mexico city, Atmos. Environ., 273, 118964, https://doi.org/10.1016/j.atmosenv.2022.118964, 2022.

Chen, J., Wu, Z., Augustin-Bauditz, S., Grawe, S., Hartmann, M., Pei, X., Liu, Z., Ji, D., and Wex, H.: Ice-nucleating particle concentrations unaffected by urban air pollution in Beijing, China, Atmos. Chem. Phys., 18, 3523–3539, https://doi.org/10.5194/acp-18-3523-2018, 2018.

Chen, J., Wu, Z., Chen, J., Reicher, N., Fang, X., Rudich, Y., and Hu, M.: Size-resolved atmospheric ice-nucleating particles during East Asian dust events, Atmos. Chem. Phys., 21, 3491–3506, https://doi.org/10.5194/acp-21-3491-2021, 2021.

Chen, J., Wu, Z., Meng, X., Zhang, C., Chen, J., Qiu, Y., Chen, L., Fang, X., Wang, Y., Zhang, Y., Chen, S., Gao, J., Li, W., and Hu, M.: Observational Evidence for the Non-Suppression Effect of Atmospheric Chemical Modification on the Ice Nucleation Activity of East Asian Dust, Sci. Total Environ., 861, 160708, https://doi.org/10.1016/j.scitotenv.2022.160708, 2023.

Chen, J., Wu, Z., Gong, X., Qiu, Y., Chen, S., Zeng, L., and Hu, M.: Anthropogenic Dust as a Significant Source of Ice-Nucleating Particles in the Urban Environment, Earths Future, 12, e2023EF003738, https://doi.org/10.1029/2023EF003738, 2024.

Connolly, P. J., Möhler, O., Field, P. R., Saathoff, H., Burgess, R., Choularton, T., and Gallagher, M.: Studies of heterogeneous freezing by three different desert dust samples, Atmos. Chem. Phys., 9, 2805–2824, https://doi.org/10.5194/acp-9-2805-2009, 2009.

David, R. O., Marcolli, C., Fahrni, J., Qiu, Y., Perez Sirkin, Y. A., Molinero, V., Mahrt, F., Brühwiler, D., Lohmann, U., and Kanji, Z. A.: Pore condensation and freezing is responsible for ice formation below water saturation for porous particles, P. Natl. Acad. Sci. USA, 116, 8184–8189, https://doi.org/10.1073/pnas.1813647116, 2019.

De Leo, V., Catucci, L., Di Mauro, A. E., Agostiano, A., Giotta, L., Trotta, M., and Milano, F.: Effect of ultrasound on the function and structure of a membrane protein: The case study of photosynthetic Reaction Center from Rhodobacter sphaeroides, Ultrason. Sonochem., 35, 103–111, https://doi.org/10.1016/j.ultsonch.2016.09.007, 2017.

DeMott, P. J., Prenni, A. J., Liu, X., Kreidenweis, S. M., Petters, M. D., Twohy, C. H., Richardson, M. S., Eidhammer, T., and Rogers, D. C.: Predicting global atmospheric ice nuclei distributions and their impacts on climate, P. Natl. Acad. Sci. USA, 107, 11217–11222, https://doi.org/10.1073/pnas.0910818107, 2010.

DeMott, P. J., Prenni, A. J., McMeeking, G. R., Sullivan, R. C., Petters, M. D., Tobo, Y., Niemand, M., Möhler, O., Snider, J. R., Wang, Z., and Kreidenweis, S. M.: Integrating laboratory and field data to quantify the immersion freezing ice nucleation activity of mineral dust particles, Atmos. Chem. Phys., 15, 393–409, https://doi.org/10.5194/acp-15-393-2015, 2015.

Engelstaedter, S., Tegen, I., and Washington, R.: North African dust emissions and transport, Earth-Sci. Rev., 79, 73–100, https://doi.org/10.1016/j.earscirev.2006.06.004, 2006.

Harrison, A. D., Lever, K., Sanchez-Marroquin, A., Holden, M. A., Whale, T. F., Tarn, M. D., McQuaid, J. B., and Murray, B. J.: The ice-nucleating ability of quartz immersed in water and its atmospheric importance compared to K-feldspar, Atmos. Chem. Phys., 19, 11343–11361, https://doi.org/10.5194/acp-19-11343-2019, 2019.

Hoose, C. and Möhler, O.: Heterogeneous ice nucleation on atmospheric aerosols: a review of results from laboratory experiments, Atmos. Chem. Phys., 12, 9817–9854, https://doi.org/10.5194/acp-12-9817-2012, 2012.

Hu, Y., Tian, P., Huang, M., Bi, K., Schneider, J., Umo, N. S., Ullmerich, N., Höhler, K., Jing, X., Xue, H., Ding, D., Liu, Y., Leisner, T., and Möhler, O.: Characteristics of ice-nucleating particles in Beijing during spring: A comparison study of measurements between the suburban and a nearby mountain area, Atmos. Environ., 293, 119451, https://doi.org/10.1016/j.atmosenv.2022.119451, 2023.

Huang, Y., Adebiyi, A. A., Formenti, P., and Kok, J. F.: Linking the Different Diameter Types of Aspherical Desert Dust Indicates That Models Underestimate Coarse Dust Emission, Geophys. Res. Lett., 48, e2020GL092054, https://doi.org/10.1029/2020GL092054, 2021.

Intergovernmental Panel on Climate Change (IPCC) (Ed.): Clouds and Aerosols, in: Climate Change 2013 – The Physical Science Basis: Working Group I Contribution to the Fifth Assessment Report of the Intergovernmental Panel on Climate Change, Cambridge University Press, Cambridge, 571–658, https://doi.org/10.1017/CBO9781107415324.016, 2014.

Jahn, L. G., Polen, M. J., Jahl, L. G., Brubaker, T. A., Somers, J., and Sullivan, R. C.: Biomass combustion produces ice-active minerals in biomass-burning aerosol and bottom ash, P. Natl. Acad. Sci. USA, 117, 21928–21937, https://doi.org/10.1073/pnas.1922128117, 2020.

Jung, S., Tiwari, M. K., and Poulikakos, D.: Frost halos from supercooled water droplets, P. Natl. Acad. Sci. USA, 109, 16073–16078, https://doi.org/10.1073/pnas.1206121109, 2012.

Kanji, Z. A., Ladino, L. A., Wex, H., Boose, Y., Burkert-Kohn, M., Cziczo, D. J., and Krämer, M.: Overview of Ice Nucleating Particles, Meteor. Mon., 58, 1.1–1.33, https://doi.org/10.1175/AMSMONOGRAPHS-D-16-0006.1, 2017.

Kanji, Z. A., Welti, A., Corbin, J. C., and Mensah, A. A.: Black Carbon Particles Do Not Matter for Immersion Mode Ice Nucleation, Geophys. Res. Lett., 47, e2019GL086764, https://doi.org/10.1029/2019GL086764, 2020.

Karagulian, F., Belis, C. A., Dora, C. F. C., Prüss-Ustün, A. M., Bonjour, S., Adair-Rohani, H., and Amann, M.: Contributions to cities' ambient particulate matter (PM): A systematic review of local source contributions at global level, Atmos. Environ., 120, 475–483, https://doi.org/10.1016/j.atmosenv.2015.08.087, 2015.

Ladino, L. A., Raga, G. B., Alvarez-Ospina, H., Andino-Enríquez, M. A., Rosas, I., Martínez, L., Salinas, E., Miranda, J., Ramírez-Díaz, Z., Figueroa, B., Chou, C., Bertram, A. K., Quintana, E. T., Maldonado, L. A., García-Reynoso, A., Si, M., and Irish, V. E.: Ice-nucleating particles in a coastal tropical site, Atmos. Chem. Phys., 19, 6147–6165, https://doi.org/10.5194/acp-19-6147-2019, 2019.

Li, F., Yan, J., Wei, Y., Zeng, J., Wang, X., Chen, X., Zhang, C., Li, W., Chen, M., and Lü, G.: $PM_{2.5}$-bound heavy metals from the major cities in China: Spatiotemporal distribution, fuzzy exposure assessment and health risk management, J. Clean. Prod., 286, 124967, https://doi.org/10.1016/j.jclepro.2020.124967, 2021.

Lohmann, U. and Feichter, J.: Global indirect aerosol effects: a review, Atmos. Chem. Phys., 5, 715–737, https://doi.org/10.5194/acp-5-715-2005, 2005.

Lohmann, U., Lüönd, F., and Mahrt, F.: An Introduction to Clouds: From the Microscale to Climate, Cambridge University Press, Cambridge, https://doi.org/10.1017/CBO9781139087513, 2016.

Marcolli, C.: Deposition nucleation viewed as homogeneous or immersion freezing in pores and cavities, Atmos. Chem. Phys., 14, 2071–2104, https://doi.org/10.5194/acp-14-2071-2014, 2014.

Marguí, E., Queralt, I., and de Almeida, E.: X-ray fluorescence spectrometry for environmental analysis: Basic principles, instrumentation, applications and recent trends, Chemosphere, 303, 135006, https://doi.org/10.1016/j.chemosphere.2022.135006, 2022.

McCluskey, C. S., DeMott, P. J., Prenni, A. J., Levin, E. J. T., McMeeking, G. R., Sullivan, A. P., Hill, T. C. J., Nakao, S., Carrico, C. M., and Kreidenweis, S. M.: Characteristics of atmospheric ice nucleating particles associated with biomass burning in the US: Prescribed burns and wildfires, J. Geophys. Res.-Atmos., 119, 10458–10470, https://doi.org/10.1002/2014JD021980, 2014.

Murray, B. J., O'Sullivan, D., Atkinson, J. D., and Webb, M. E.: Ice nucleation by particles immersed in supercooled cloud droplets, Chem. Soc. Rev., 41, 6519–6554, https://doi.org/10.1039/C2CS35200A, 2012.

Niedermeier, D., Hartmann, S., Clauss, T., Wex, H., Kiselev, A., Sullivan, R. C., DeMott, P. J., Petters, M. D., Reitz, P., Schneider, J., Mikhailov, E., Sierau, B., Stetzer, O., Reimann, B., Bundke, U., Shaw, R. A., Buchholz, A., Mentel, T. F., and Stratmann, F.: Experimental study of the role of physicochemical surface processing on the IN ability of mineral dust particles, Atmos. Chem. Phys., 11, 11131–11144, https://doi.org/10.5194/acp-11-11131-2011, 2011.

Niemand, M., Möhler, O., Vogel, B., Vogel, H., Hoose, C., Connolly, P., Klein, H., Bingemer, H., DeMott, P., Skrotzki, J., and Leisner, T.: A Particle-Surface-Area-Based Parameterization of Immersion Freezing on Desert Dust Particles, J. Atmos. Sci., 69, 3077–3092, https://doi.org/10.1175/JAS-D-11-0249.1, 2012.

O'Sullivan, D., Murray, B. J., Ross, J. F., and Webb, M. E.: The adsorption of fungal ice-nucleating proteins on mineral dusts: a terrestrial reservoir of atmospheric ice-nucleating particles, Atmos. Chem. Phys., 16, 7879–7887, https://doi.org/10.5194/acp-16-7879-2016, 2016.

O'Sullivan, D., Adams, M. P., Tarn, M. D., Harrison, A. D., Vergara-Temprado, J., Porter, G. C. E., Holden, M. A., Sanchez-Marroquin, A., Carotenuto, F., Whale, T. F., McQuaid, J. B., Walshaw, R., Hedges, D. H. P., Burke, I. T., Cui, Z., and Murray, B. J.: Contributions of biogenic material to the atmospheric ice-nucleating particle population in North Western Europe, Sci. Rep.-UK, 8, 13821, https://doi.org/10.1038/s41598-018-31981-7, 2018.

Peters, T. M., Ott, D., and O'Shaughnessy, P. T.: Comparison of the Grimm 1.108 and 1.109 Portable Aerosol Spectrometer to the TSI 3321 Aerodynamic Particle Sizer for Dry Particles, Ann. Occup. Hyg., 50, 843–850, https://doi.org/10.1093/annhyg/mel067, 2006.

Petters, M. D. and Wright, T. P.: Revisiting ice nucleation from precipitation samples, Geophys. Res. Lett., 42, 8758–8766, https://doi.org/10.1002/2015GL065733, 2015.

Polen, M., Lawlis, E., and Sullivan, R. C.: The unstable ice nucleation properties of Snomax® bacterial particles, J. Geophys. Res.-Atmos., 121, 11666–11678, https://doi.org/10.1002/2016JD025251, 2016.

Price, H. C., Baustian, K. J., McQuaid, J. B., Blyth, A., Bower, K. N., Choularton, T., Cotton, R. J., Cui, Z., Field, P. R., Gallagher, M., Hawker, R., Merrington, A., Miltenberger, A., Neely III, R. R., Parker, S. T., Rosenberg, P. D., Taylor, J. W., Trembath, J., Vergara-Temprado, J., Whale, T. F., Wilson, T. W., Young, G., and Murray, B. J.: Atmospheric Ice-Nucleating Particles in the Dusty Tropical Atlantic, J. Geophys. Res.-Atmos., 123, 2175–2193, https://doi.org/10.1002/2017JD027560, 2018.

Pummer, B. G., Budke, C., Augustin-Bauditz, S., Niedermeier, D., Felgitsch, L., Kampf, C. J., Huber, R. G., Liedl, K. R., Loerting, T., Moschen, T., Schauperl, M., Tollinger, M., Morris, C. E., Wex, H., Grothe, H., Pöschl, U., Koop, T., and Fröhlich-Nowoisky, J.: Ice nucleation by water-soluble macromolecules, Atmos. Chem. Phys., 15, 4077–4091, https://doi.org/10.5194/acp-15-4077-2015, 2015.

Reicher, N., Budke, C., Eickhoff, L., Raveh-Rubin, S., Kaplan-Ashiri, I., Koop, T., and Rudich, Y.: Size-dependent ice nucleation by airborne particles during dust events in the eastern Mediterranean, Atmos. Chem. Phys., 19, 11143–11158, https://doi.org/10.5194/acp-19-11143-2019, 2019.

Rumsey, I. C. and Walker, J. T.: Application of an online ion-chromatography-based instrument for gradient flux measurements of speciated nitrogen and sulfur, Atmos. Meas. Tech., 9, 2581–2592, https://doi.org/10.5194/amt-9-2581-2016, 2016.

Rumsey, I. C., Cowen, K. A., Walker, J. T., Kelly, T. J., Hanft, E. A., Mishoe, K., Rogers, C., Proost, R., Beachley, G. M., Lear, G., Frelink, T., and Otjes, R. P.: An assessment of the performance of the Monitor for AeRosols and GAses in ambient air (MARGA): a semi-continuous method for soluble compounds, Atmos. Chem. Phys., 14, 5639–5658, https://doi.org/10.5194/acp-14-5639-2014, 2014.

Stein, A. F., Draxler, R. R., Rolph, G. D., Stunder, B. J. B., Cohen, M. D., and Ngan, F.: NOAA's HYSPLIT Atmospheric Transport and Dispersion Modeling System, B. Am. Meteorol. Soc., 96, 2059–2077, https://doi.org/10.1175/BAMS-D-14-00110.1, 2015.

Su, H., Yin, Y., Lu, C., Jiang, H., and Yang, L.: Development of new diffusion cloud chamber type and its observation study of ice nuclei in the Huangshan area, Chinese Journal of Atmospheric Sciences, 38, 386–398, https://doi.org/10.3878/j.issn.1006-9895.2013.12211, 2014 (in Chinese).

Tobo, Y., Uetake, J., Matsui, H., Moteki, N., Uji, Y., Iwamoto, Y., Miura, K., and Misumi, R.: Seasonal Trends of Atmospheric Ice Nucleating Particles Over Tokyo, J. Geophys. Res.-Atmos., 125, e2020JD033658, https://doi.org/10.1029/2020JD033658, 2020.

Toll, V., Rahu, J., Keernik, H., Trofimov, H., Voormansik, T., Manshausen, P., Hung, E., Michelson, D., Christensen, M. W., Post, P., Junninen, H., Murray, B. J., Lohmann, U., Watson-Parris, D., Stier, P., Donaldson, N., Storelvmo, T., Kulmala, M., and Bellouin, N.: Glaciation of liquid clouds, snowfall, and reduced cloud cover at industrial aerosol hot spots, Science, 386, 756–762, https://doi.org/10.1126/science.adl0303, 2024.

US EPA: EPA Positive Matrix Factorization 5.0 Fundamentals and User Guide, https://www.epa.gov/air-research/epa-positive-matrix-factorization-50-fundamentals-and-user-guide (last access: 10 October 2025), 2015.

Vali, G., DeMott, P. J., Möhler, O., and Whale, T. F.: Technical Note: A proposal for ice nucleation terminology, Atmos. Chem. Phys., 15, 10263–10270, https://doi.org/10.5194/acp-15-10263-2015, 2015.

Wagh, S., Singh, P., Ghude, S. D., Safai, P., Prabhakaran, T., and Kumar, P. P.: Study of ice nucleating particles in fog-haze weather at New Delhi, India: A case of polluted environment, Atmos. Res., 259, 105693, https://doi.org/10.1016/j.atmosres.2021.105693, 2021.

Wan, Z., Song, K., Zhu, W., Yu, Y., Wang, H., Shen, R., Tan, R., Lv, D., Gong, Y., Yu, X., Chen, S., Zeng, L., Lou, S., Yu, Y., and Guo, S.: A Closure Study of Secondary Organic Aerosol Estimation at an Urban Site of Yangtze River Delta, China, Atmosphere-Basel, 13, 1679, https://doi.org/10.3390/atmos13101679, 2022.

Wang, Y. Q.: MeteoInfo: GIS software for meteorological data visualization and analysis, Meteorol. Appl., 21, 360–368, https://doi.org/10.1002/met.1345, 2014.

Westbrook, C. D. and Illingworth, A. J.: The formation of ice in a long-lived supercooled layer cloud, Q. J. Roy. Meteor. Soc., 139, 2209–2221, https://doi.org/10.1002/qj.2096, 2013.

Wiedensohler, A.: An approximation of the bipolar charge distribution for particles in the submicron size range, J. Aerosol Sci., 19, 387–389, https://doi.org/10.1016/0021-8502(88)90278-9, 1988.

Yahya, R. Z., Arrieta, J. M., Cusack, M., and Duarte, C. M.: Airborne Prokaryote and Virus Abundance Over the Red Sea, Front. Microbiol., 10, 1112, https://doi.org/10.3389/fmicb.2019.01112, 2019.

Yang, J., Chen, J., Chen, J., Feng, Z., Fang, W., Qiu, Y., Wang, J., Man, R., Zong, T., Liu, Y., Wu, Z., Tang, N., and Hu, M.: Dataset for atmospheric ice-nucleating particles in urban Taiyuan during winter 2023–2024, Zenodo [data set], https://doi.org/10.5281/zenodo.20232172, 2026.

Zhang, C., Wu, Z., Chen, J., Chen, J., Tang, L., Zhu, W., Pei, X., Chen, S., Tian, P., Guo, S., Zeng, L., Hu, M., and Kanji, Z. A.: Ice-nucleating particles from multiple aerosol sources in the urban environment of Beijing under mixed-phase cloud conditions, Atmos. Chem. Phys., 22, 7539–7556, https://doi.org/10.5194/acp-22-7539-2022, 2022.

Zolles, T., Burkart, J., Häusler, T., Pummer, B., Hitzenberger, R., and Grothe, H.: Identification of Ice Nucleation Active Sites on Feldspar Dust Particles, J. Phys. Chem. A, 119, 2692–2700, https://doi.org/10.1021/jp509839x, 2015.